atmosphere

MDPI

Article

An Analysis of Meteorological Anomalies in Kamchatka in Connection with the Seismic Process

Alexey Lyubushin [1,*], Galina Kopylova [2], Eugeny Rodionov [1] and Yulia Serafimova [2]

[1] Schmidt Institute of Physics of the Earth, Russian Academy of Sciences, 123995 Moscow, Russia; evgeny_980@list.ru
[2] Kamchatka Branch of the Geophysical Survey of the Russian Academy of Sciences (KB GS RAS), 683023 Petropavlovsk-Kamchatsky, Russia; gala@emsd.ru (G.K.); yulka@emsd.ru (Y.S.)
* Correspondence: lyubushin@yandex.ru

Abstract: This study investigates the hypothesis that meteorological anomalies may precede earthquake events. Long-term time series of observations for air temperature, atmospheric pressure and precipitation at a meteorological station in Kamchatka are considered. Time series are subjected to Huang decomposition into sequences of levels of empirical oscillation modes (intrinsic mode functions—IMFs), forming a set of orthogonal components with decreasing average frequency. For each IMF level, the instantaneous amplitudes of envelopes are calculated using the Hilbert transform. A comparison with the earthquake sequence is made using a parametric model of the intensity of two interacting point processes, which allows one to quantitatively estimate the "measure of the lead" of the time instants of the compared sequences. For each IMF level, the number of time moments of the largest local maxima of instantaneous amplitudes which is equal to the number of earthquakes is selected. As a result of the analysis, it turned out that for the sixth IMF level (periods of 8–16 days), the "lead measure" of the instantaneous amplitude maxima of meteorological parameters in comparison with earthquake time moments significantly exceeds the inverse lead, which confirms the existence of prognostic changes in meteorological parameters in the problem of "atmosphere–lithosphere" interaction. This study reveals that certain meteorological anomalies can be a precursor for seismic activity.

Keywords: atmosphere–lithosphere interaction; meteorological time series; seismic process; Hilbert–Huang decomposition; instantaneous amplitudes; interacting point processes; Kamchatka

Academic Editor: Masashi Hayakawa

Received: 22 December 2024
Revised: 7 January 2025
Accepted: 10 January 2025
Published: 13 January 2025

Citation: Lyubushin, A.; Kopylova, G.; Rodionov, E.; Serafimova, Y. An Analysis of Meteorological Anomalies in Kamchatka in Connection with the Seismic Process. *Atmosphere* **2025**, *16*, 78. https://doi.org/10.3390/atmos16010078

1. Introduction

In the study of the interaction of processes at the lithosphere–atmosphere boundary, one intriguing aspect to consider is the study of the relationship between the variability in meteorological conditions in the near-surface conditions of the Earth and the final stages of the preparation processes for strong earthquakes. The consideration of this question is especially relevant in relation to the problem of forecasting earthquakes based on possible meteorological precursors.

A number of publications have demonstrated the effects of the increasing temperature and decreasing humidity of the surface air of the atmosphere before strong and moderate earthquakes [1–6]. An explanation of this phenomenon is given within the framework of the model of complex relationships in the lithosphere–atmosphere and ionosphere–magnetosphere (LAIMC) system [7]. According to the LAIMC system, at the final relatively short-term stage of earthquake preparation, thermal anomalies in the atmosphere at low

altitudes may form due to the release of the latent heat of evaporation during the condensation of water vapor on ions due to the ionization of air molecules caused by alpha particles emitted by the nuclei of radioactive gases, mainly radon, entering the atmosphere from the upper horizons of the Earth's crust.

The verification of the LAIMC model requires the presence of indisputable data on the occurrence of anomalous radon flows from the Earth's surface on the eve of strong earthquakes or on establishing a connection between data from long-term meteorological observations in seismically active regions, in particular data on surface air temperature, and earthquakes that have occurred.

Observations of the volumetric activity of radon in near-surface conditions are usually of an experimental nature. In addition to reports of the phenomenon of an increase in the volumetric activity of soil gaseous radon, there are also data on a decrease in its activity before earthquakes [8,9]. Therefore, the question of the occurrence of anomalous discharges of gaseous radon from the lithosphere into the atmosphere before strong earthquakes remains unanswered to this day.

The study of various types of earthquake precursors in the Kamchatka Peninsula area shows that the characteristic durations of their manifestation before earthquakes range from days to months to a few years [10–18]. This demonstrates the need to develop methods for analyzing the relationship between meteorological parameters and the seismic process, allowing such a relationship to be analyzed in a wide range of periods of its manifestation, including the months and years preceding strong Kamchatka earthquakes.

A promising development in studying processes at the lithosphere–atmosphere boundary during earthquake preparation is the use of long-term meteorological observations in seismically active regions. Such observations are carried out on the basis of metrologically supported methods for issuing weather forecasts, assessing the state of the natural environment, etc. In Ref. [19], using observational data from meteorological stations in the seismically active region of the Kamchatka Peninsula, the authors analyzed the relationship between increased and decreased values of air temperature and atmospheric pressure, as well as their contrasting changes, at the final stages of preparation for local strong earthquakes accompanied by noticeable tremors. In this work, an empirical method of comparing average daily values with the behavior of annual average seasonal functions was used to identify anomalous changes in meteorological parameters. In addition, formalized statistical methods were used to identify anomalies in the behavior of three statistics characterizing the variability in the time series of air temperature and atmospheric pressure in a sliding time window of 112 days with a step of 1 day. Using empirical and statistical methods for processing the time series of meteorological parameters, anomalous effects were identified at time intervals of 7, 30 and 112 days, and so was their seismic forecasting significance in relation to the strong earthquakes that occurred. The detection of the random nature of the manifestation of various types of meteorological anomalies before the earthquakes under consideration, as well as the absence of the systematic manifestation of the effects of an abnormal increase in air temperature before earthquakes, cast doubt on the realism of generating thermal near-surface anomalies of atmospheric air at the short-term stage of preparation for strong seismic events in the Kamchatka region.

It should be noted that in Ref. [19], the assignment of time intervals of 7, 30 and 112 days, during which the manifestation of a relationship between surface meteorological anomalies and earthquake preparation processes was assumed, was conducted on the assumption of the presence of a relatively short-term manifestation of thermal effects before strong earthquakes.

In this paper, the Huang method was used to decompose long-term meteorological time series, which allows the construction of a sequence of orthogonal oscillations for

each series, which are called "internal oscillation modes" in the method. The Hilbert transform of the sequence of these oscillation modes makes it possible to obtain sequences of instantaneous amplitudes and frequencies. The paper studies the relationship between the time points of maxima of instantaneous amplitudes of meteorological parameter series and the time moments of strong earthquakes using a parametric model of interacting point processes. The result of the study is the discovery of the effect of leading the time points of the maxima of instantaneous amplitudes of air temperature of the time moments of earthquakes at the low-frequency level of the Huang decomposition.

The novelty of the used method of joint analysis of meteorological time series and seismicity lies in the joint use of the Hilbert–Huang decomposition and the influence matrix method to assess the relationship between two point processes.

2. Initial Data

The work used meteorological observation data and data on earthquakes that occurred in the Kamchatka Peninsula region for the period from 4 November 1996 to 30 September 2024 (10,193 days), a total of 27 years 11 months (27.9 years).

2.1. Meteorological Data

The data of observations of atmospheric pressure, air temperature and precipitation at the Pionerskaya meteorological station of the Kamchatka Territorial Administration for Hydrometeorology and Environmental Monitoring (53.08° N, 158.55° E) from the database of the POLYGON Information System of the Kamchatka Branch of the Geophysical Service of the Russian Academy of Sciences were used [20].

At the Pionerskaya meteorological station, a meteorological mercury thermometer with a division value of 0.2 °C is used to measure the air temperature. It is located in a protective wooden booth at a height of 2 m above the Earth's surface. Atmospheric pressure was measured with a mercury barometer. Precipitation was measured with a precipitation vessel installed on a horizontal surface at a height of 2 m and protected from gusts of wind. The amount of precipitation is the height of the water layer in mm formed by rain, drizzle, melted snow and hail.

The sampling step of meteorological observations and the corresponding discretization of time series of meteorological parameters is 3 h (Figure 1).

2.2. Earthquake Data

To characterize the seismic process in the Kamchatka Peninsula area during the period from 4 November 1996 to 30 September 2024, a sample of 418 earthquakes with local magnitudes that occurred in the depth range from 0 to 635 km in the responsibility area of the Kamchatka Branch of the Geophysical Survey of the Russian Academy of Sciences (KB GS RAS) was used. The earthquake sampling was carried out from the Kamchatka and Commander Islands Earthquake Catalogue: (http://www.gsras.ru/new/infres/, [ID 85], accessed 1 October 2024) using the Unified Information System of Seismological Data KB GS RAS [21] and the Interactive Map of the Distribution of Earthquake Epicenters from the Kamchatka and Commander Islands Earthquake Catalogue (see https://sdis.emsd.ru/map/, accessed on 15 December 2024).

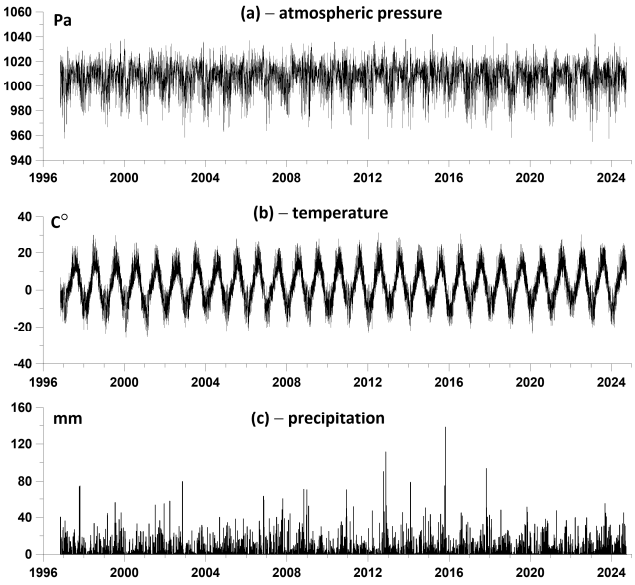

Figure 1. Initial data—atmospheric pressure (**a**), air temperature (**b**) and precipitation (**c**) at the Pionerskaya weather station, 4 November 1996–30 September 2024, with a time step of 3 h, giving 81,544 readings.

Figure 2 shows the epicenters of all 418 earthquakes, the boundaries of the KB GS RAS area of responsibility and the location of the Pionerskaya weather station.

In the catalog of Kamchatka and the Commander Islands compiled by KB GS RAS, the representative energy class of earthquakes (decimal logarithm of seismic energy output) for the entire responsibility zone is $K = 11.5$ and corresponds to the local magnitude $M_L = 5.0$. To obtain the studied sample of earthquakes, earthquakes with $K = 12.5$ for the considered time period were selected from the specified catalog. The magnitudes M_L in the sample of earthquakes were recalculated from the values of the energy classes K using the formula $M_L = 0.5K - 0.75$ [22]. Thus, setting the minimum magnitude $M_L = 5.5$ obviously ensured the representativeness of the resulting sample of 418 earthquakes for the entire territory of the KB GS RAS responsibility zone.

The 418 earthquakes under consideration have magnitudes $M_L = 5.5 - 7.8$. Table 1 presents data on the strongest earthquakes that occurred according to KB GS RAS data and data on their moment magnitudes M_W from the USGS/NEIS catalog.

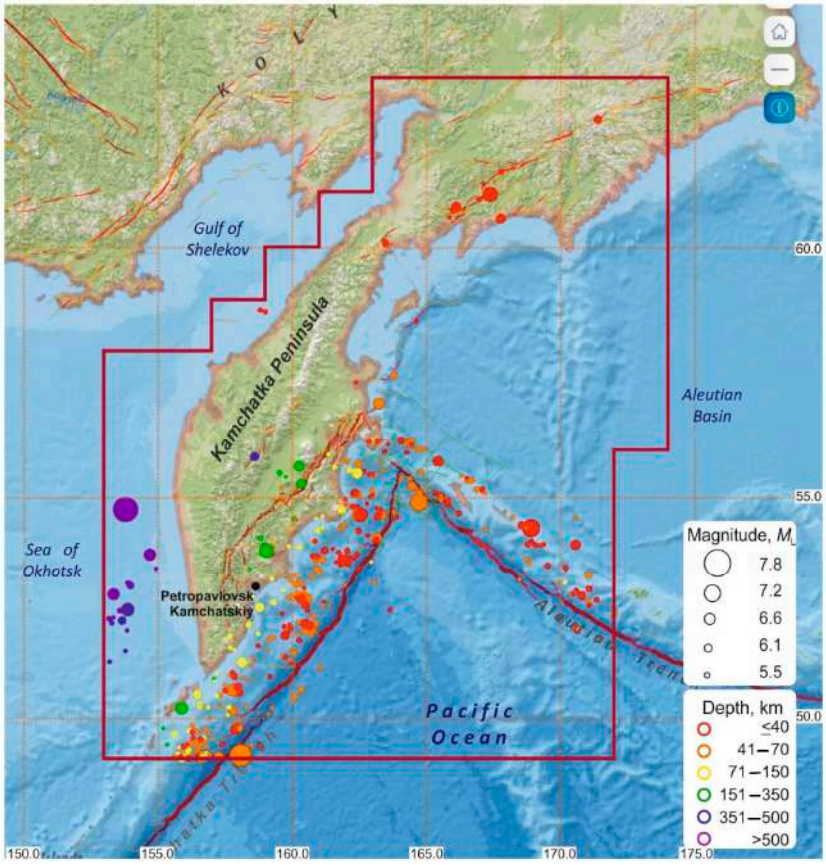

Figure 2. Map of epicenters of 418 earthquakes with $M_L \geq 5.5$ that occurred in the KB GS RAS responsibility area (area bounded by the red line) from 4 November 1996 to 30 September 2024, and the location of the Pionerskaya weather station (black circle). Red lines are active faults according to [23].

Table 1. Data on the strongest ($M_W \geq 6.5$) earthquakes that occurred in the KB GS RAS area of responsibility according to https://sdis.emsd.ru/info/earthquakes/catalogue.php, https://earthquake.usgs.gov/earthquakes/search/, accessed on 15 December 2024.

Date dd.mm.yyyy	Time hh:mm:ss	Latitude, N°	Longitude, E°	Depth, km	M_L	R, km	M_W NEIC	L, km	R/L
16.06.2003	22:08:02	55.30	160.34	190	6.6	331	6.9	50	6.7
05.12.2003	21:26:14	55.78	165.43	29	6.7	533	6.7	41	13.1
10.06.2004	15:19:55	55.68	160.25	208	6.7	370	6.9	50	7.4
20.04.2006	23:24:28	60.98	167.37	1	7.1	1019	7.6	100	10.2
24.11.2008	9:02:52	53.77	154.69	564	6.8	623	7.3	74	8.4
16.11.2012	18:12:39	49.06	155.87	78	6.7	486	6.5	33	14.5
28.02.2013	1:05:48	50.67	157.77	61	6.8	271	6.9	50	5.4
01.03.2013	13:20:49	50.64	157.90	62	6.8	272	6.5	33	8.1
24.05.2013	5:44:47	54.75	153.79	630	7.8	726	8.3	199	3.6
01.10.2013	3:38:19	52.88	153.34	608	6.8	700	6.7	41	17.1
30.01.2016	3:25:08	53.85	159.04	178	7.1	200	7.2	67	3.0
29.03.2017	4:09:22	56.97	163.22	43	6.8	521	6.6	37	14.1
02.06.2017	22:24:47	53.99	170.55	32	6.6	795	6.8	45	17.6

Table 1. *Cont.*

Date dd.mm.yyyy	Time hh:mm:ss	Latitude, N°	Longitude, E°	Depth, km	M_L	R, km	M_W NEIC	L, km	R/L
17.07.2017	23:34:08	54.35	168.90	7	7.3	692	7.7	110	6.3
13.10.2018	11:10:20	52.53	153.87	499	7.0	592	6.7	41	14.5
20.12.2018	17:01:54	54.91	164.71	54	7.3	448	7.3	74	6.1
25.03.2020	2:49:20	49.11	158.08	48	7.7	438	7.5	90	4.9
03.04.2023	3:06:56	52.58	158.78	105	6.6	120	6.5	33	3.6
17.08.2024	19:10:25	52.79	160.38	43	7.0	126	7.0	55	2.3

Note: R is the hypocentral distance to the Pionerskaya weather station and L is the size of the earthquake source, calculated using the formula $L = 10^{(0.43M_W - 1.27)}$ [24].

3. Research Method

3.1. Empirical Mode Decomposition

Let $\xi(t)$ be some analyzed time series with a discrete time index.

Empirical mode decomposition (EMD) [25,26] represents the decomposition into empirical oscillation modes:

$$\xi(t) = \sum_{k=1}^{n} G_k(t) + r_n(t) \quad (1)$$

where $G_k(t)$ is the empirical mode, having the number k, $r_n(t)$ is the remainder and n is the number of empirical modes.

Decomposing into empirical modes presents iterations for each level k. Let i be the iteration index: $i = 0, 1, \ldots, I_k$, where I_k is the number of iterations for level k. The iterations are described by the following formula:

$$g_k^{(i+1)}(t) = g_k^{(i)}(t) - \zeta_k^{(i)}(t) \quad (2)$$

Here, $\zeta_k^{(l)}(t) = \left(A_k^{(l)}(t) + B_k^{(l)}(t)\right)/2$, where $A_k^{(l)}(t)$ and $B_k^{(l)}(t)$ are the upper and lower envelopes for the signal $g_k^{(i)}(t)$, which are constructed using 3rd order spline interpolation over all local maxima and minima.

Iterations (2) are started with an initial step for the 1st level: $G_1^{(0)}(t) = \xi(t)$. Then the upper and lower envelopes $A_1^{(0)}(t)$ and $B_1^{(0)}(t)$ are found, the average line $\zeta_1^{(0)}(t)$ is calculated and $g_1^{(1)}(t)$ is found using Formula (2). For $g_1^{(1)}(t)$, the upper and lower envelopes $A_1^{(1)}(t)$ and $B_1^{(1)}(t)$ are determined and the average line $\zeta_1^{(1)}(t)$ and $g_1^{(2)}(t)$ are found, and so on, up to the last iteration index I_1, after which the first empirical mode $G_1(t) = g_1^{(I_1)}(t)$ is considered to be found.

The last iteration index I_k is defined from the following inequality:

$$\sum_t \left(g_k^{(i+1)}(t) - g_k^{(i)}(t)\right)^2 / \sum_t \left(g_k^{(i)}(t)\right)^2 \leq \eta \quad (3)$$

η is some small value, such as 0.01. Once the mode $G_k(t)$ is found, the next iterations start for the mode $G_{k+1}(t)$. This process is initialized by the formula for the initial iteration index $i = 0$:

$$g_{k+1}^{(0)}(t) = \xi(t) - G_k(t) \quad (4)$$

The empirical oscillation modes are computed until the number of local extrema becomes too small for calculating envelopes. As the empirical mode level number k increases,

the modes $G_k(t)$ become lower and lower in frequency. The sum of $G_1(t), \ldots, G_n(t)$ gives an approximation to the original signal $\xi(t)$, which can be represented as (1) [25,26].

Empirical modes of oscillations, known as Intrinsic Mode Functions (IMFs), are orthogonal, thus presenting an empirical basis for the expansion of the initial signal $\xi(t)$. In what follows, the decomposition levels will be called IMF levels. In practice, technical difficulties occur due to effects at the beginning and end of time series, since the calculation of envelopes beyond the first and last points of local extrema is ambiguous. To overcome these difficulties, we used a mirror continuation of the analyzed sample backward and forward over a sufficiently long fragment of time.

3.2. Ensemble Empirical Mode Decomposition

The main difficulty in applying the EMD decomposition is the problem of "intermittency", when the original signal includes short-term fragments of high-frequency behavior. In this case, mode mixing occurs, since rare extreme points of the low-frequency component are interspersed with frequent local extreme points of the high-frequency component. The ensemble empirical mode decomposition (EEMD) method proposed in [26] allows one to calculate the true empirical modes as an averaging of a series of decompositions of noisy signals by adding independent white noise.

The EEMD method presents the next steps:

1. A white noise realization is added to the original data.
2. The white noise-added data are decomposed into empirical modes.
3. Steps 1 and 2 are repeated a large number of times for independent white noise realizations.
4. All white-noise added empirical modes are averaged for each IMF level.

It is important to note that the use of EEMD largely eliminates the above-mentioned mode mixing problem [26]. Adding independent white noise to the sample has a regularizing effect, since it simplifies the construction of envelopes (after adding a small white noise, there are immediately many local extrema). The operation of averaging over a sufficiently large number of independent realizations of white noise allows one to get rid of the influence of the noise component and to isolate the true internal modes of oscillations of time series of meteorological parameters.

For each of the time series (Figure 1), EEMD waveforms were calculated by averaging 2000 decompositions of the original signals, to which independent Gaussian white noise with a standard deviation equal to 0.1 of the standard deviation of each decomposed signal was added.

3.3. Hilbert Transform

The Hilbert transform [27] $H_x(t)$ of a narrow-banded signal $x(t)$ is determined by the following formula:

$$H_x(t) = \int_{-\infty}^{+\infty} x(s)ds/(\pi \cdot (t-s)) \quad (5)$$

In practice, it is more convenient to calculate the Hilbert transform using an analytical signal [27]:

$$Z_x(t) = x(t) + i \cdot H_x(t) = \left|Z_x(t)\right| \cdot e^{i\varphi(t)} \equiv A_x(t) \cdot e^{i\varphi(t)} \quad (6)$$

where $A_x(t) = \sqrt{x^2(t) + H_x^2(t)}$ are the amplitudes of the signal $x(t)$ envelope, and $\varphi(t)$ is the instantaneous phase. The derivative $\nu(t) = d\varphi(t)/dt$ is the instantaneous frequency. The calculations according to Formulae (5) and (6) for time series $x(t)$ with a discrete time index could easily be performed by using a fast discrete Fourier transform [27].

Next, the Hilbert transform is applied to the sequence of empirical modes $G_1(t), \ldots, G_n(t)$ found using the EEMD method. Special attention is paid to the points of local maxima of the amplitudes of the empirical mode envelopes. The times of reaching the largest local maxima of these amplitudes will be compared with the times of earthquakes.

Thus, after determining the instantaneous amplitudes and frequencies of the EEMD, the Hilbert–Huang expansion can be represented as follows:

$$x(t) = \sum_{k=1}^{n} G_k(t) + r_n(t), \quad G_k(t) = \mathrm{Re}\left\{ A_k(t) \cdot \exp\left(i \cdot \int_0^t \nu_k(s) ds \right) \right\} \tag{7}$$

Below, in Figures 3–5, the EEMD waveform graphs are presented for Levels 1 to 12 of all time series of meteorological parameters, the amplitude graphs of their envelopes and instantaneous frequencies calculated using the Hilbert transform.

The Hilbert–Huang decomposition resembles the wavelet decomposition in its form (functionally): as in the wavelet decomposition, with an increase in the IMF level number, the corresponding component becomes increasingly low frequency. However, there is a significant difference, which lies in the dependence of both the amplitude and the frequency on time, which is expressed by Formula (7). In the orthogonal wavelet decomposition, the frequency band corresponding to the detail level with the number is fixed and corresponds to the frequency interval $[\Omega_{\min}^{(k)}, \Omega_{\max}^{(k)}]$, where $\Omega_{\min}^{(k)} = 1/(2^{(k+1)} \cdot \Delta t)$, $\Omega_{\max}^{(k)} = 1/(2^k \cdot \Delta t)$, where Δt is the discretization step in time [28]. In the Hilbert–Huang decomposition, there is no such one-to-one correspondence. Therefore, to estimate the characteristic frequency of each IMF level, a value equal to the time average of all instantaneous frequency values was used. Figure 6 shows the average values of instantaneous frequencies of meteorological parameters depending on the IMF level number.

The Hilbert–Huang method has a wide range of applications in a variety of areas of time series analysis: meteorology, geodesy, finance and so on [29–36].

3.4. Influence Matrix

The next stage of the analysis is the study of the relationship between two sequences of random events, which in this study represent the sequence of the largest local maxima of the envelopes of the initial series of meteorological parameters determined by the algorithm described above and the sequence of 418 earthquakes with $M_L \geq 5.5$.

To solve this problem, a parametric model of the intensity of two point processes is used.

Previously, in Refs. [36–38], this method was used to test the hypotheses that local extremes of the mean values of certain seismic noise and magnetic field statistics precede the times of strong earthquakes. In Ref. [36], this model was used to estimate the seismic forecasting properties of the positions of local maxima of instantaneous amplitudes of the envelopes of ground tremor on the Japanese islands, measured by GPS.

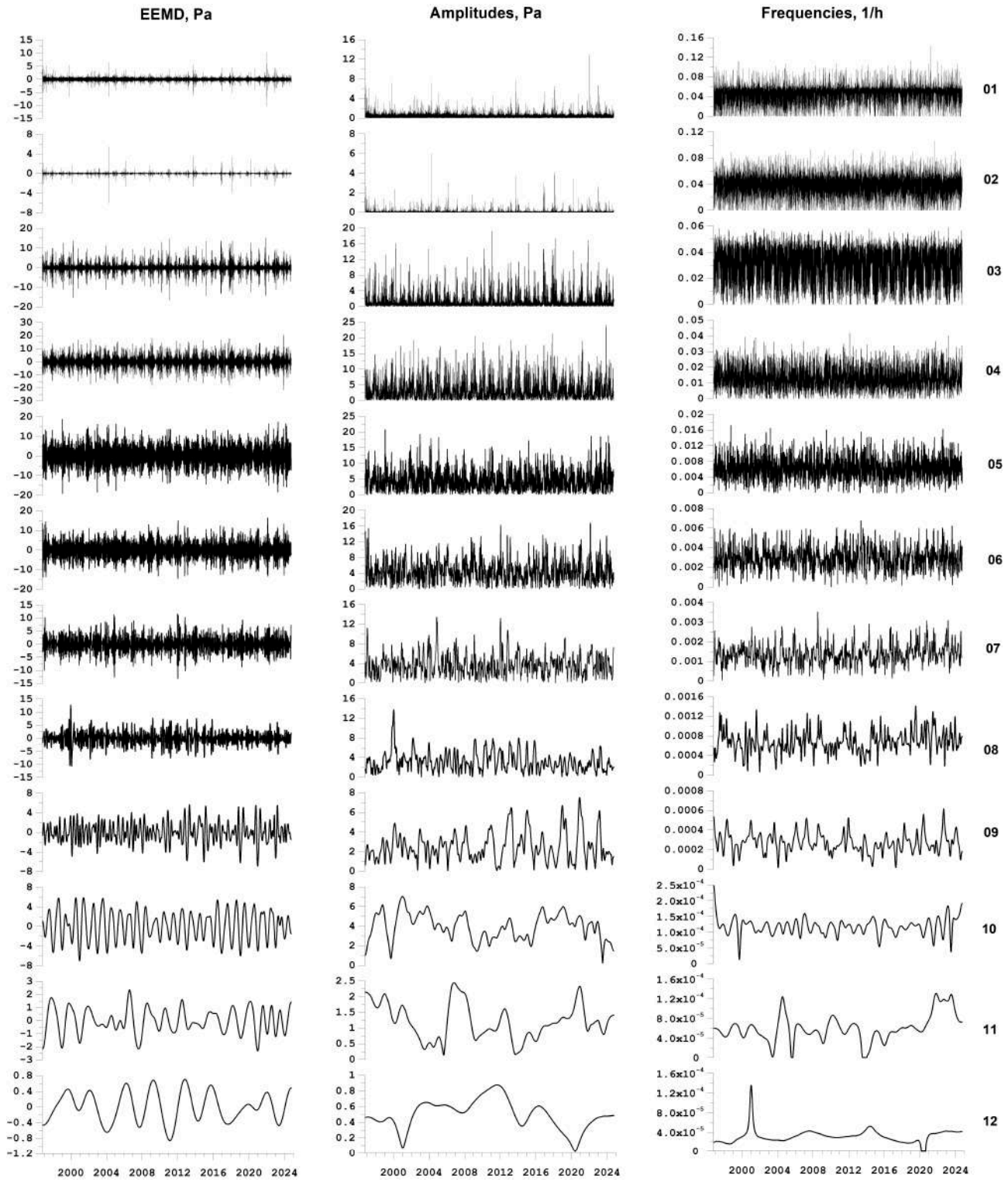

Figure 3. Waveforms of the EEMD decomposition of the atmospheric pressure series for IMF levels with numbers from 1 to 12, the amplitudes of their envelopes and instantaneous frequencies calculated using the Hilbert transform.

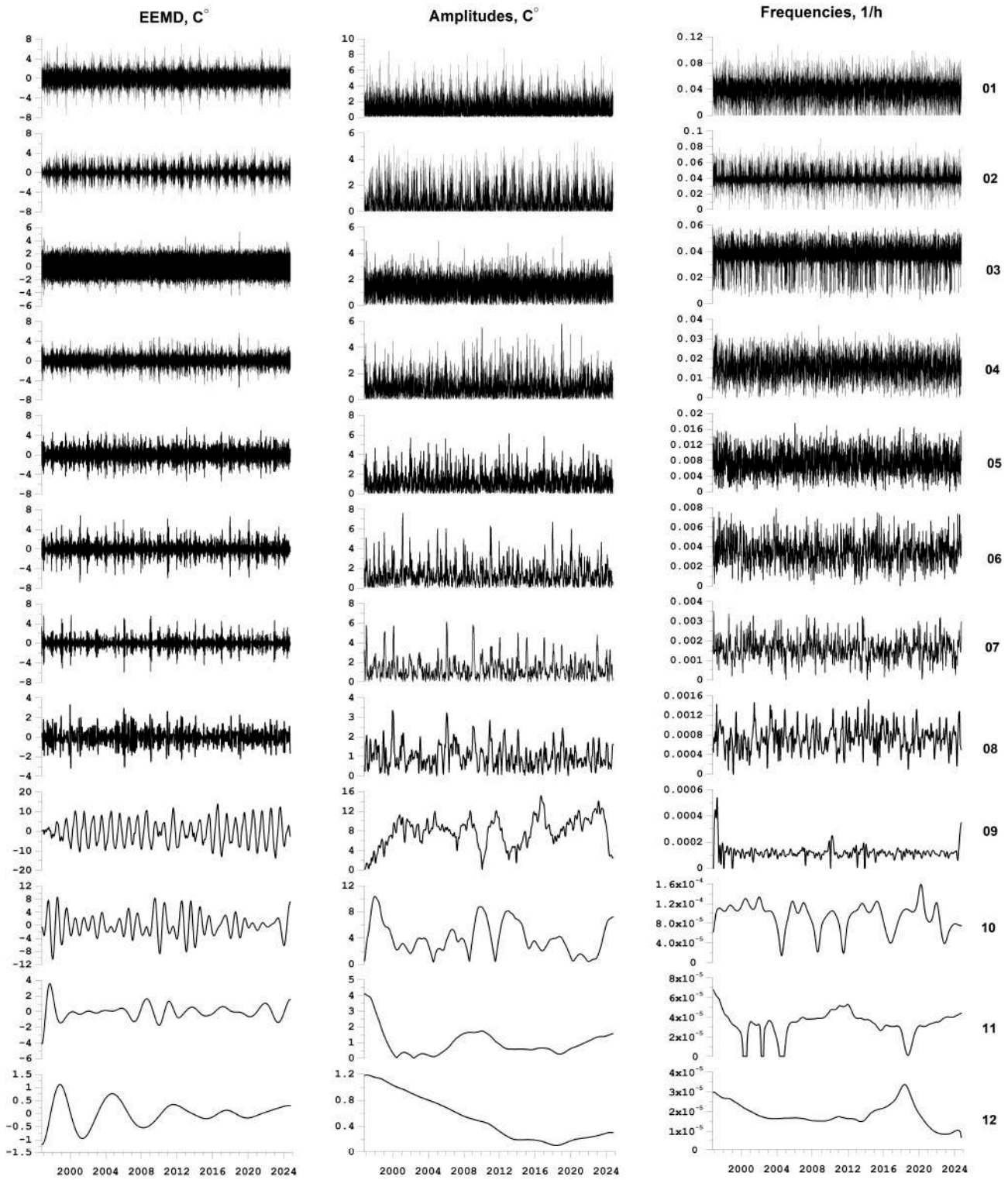

Figure 4. Waveforms of the EEMD decomposition of the air temperature series for IMF levels with numbers from 1 to 12, the amplitudes of their envelopes and instantaneous frequencies calculated using the Hilbert transform.

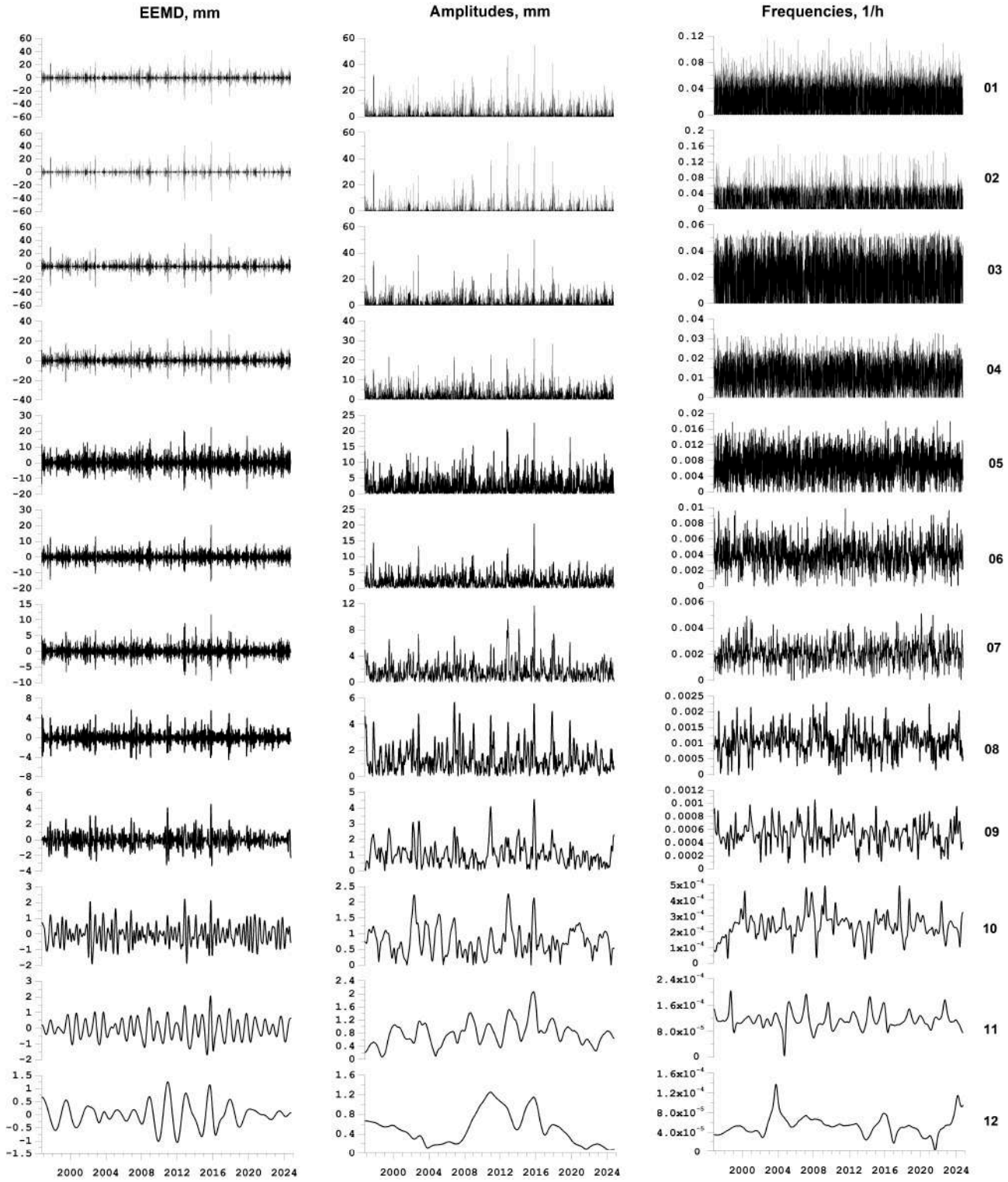

Figure 5. Waveforms of the EEMD decomposition of the precipitation series for IMF levels with numbers from 1 to 12, the amplitudes of their envelopes and instantaneous frequencies calculated using the Hilbert transform.

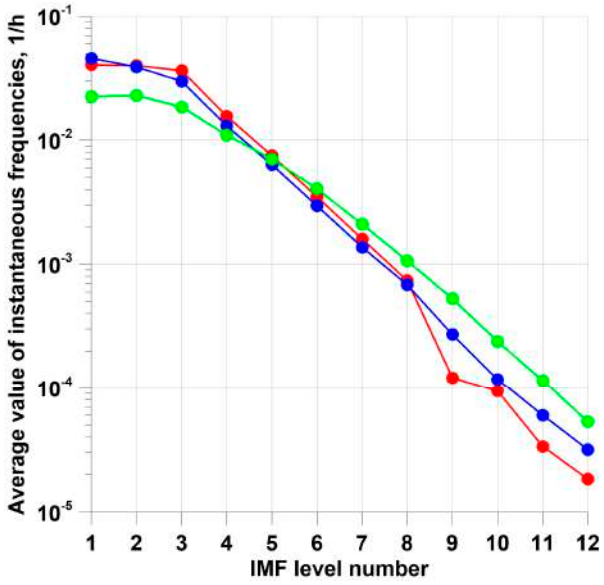

Figure 6. Average values of instantaneous frequencies depending on the IMF level number for time series of atmospheric pressure (blue), air temperature (red) and precipitation (green).

Let us consider the computational algorithm. Let $t_j^{(\alpha)}$, $j = 1, \ldots, N_\alpha$; $\alpha = 1, 2$ be the time moments of two sequences of events. In our case, these are as follows:

(1) A sequence of time moments corresponding to the largest local maxima of the envelope amplitudes at some IMF levels of the EEMD decomposition;
(2) The sequence of times of seismic events with a magnitude not less than a given value (in our case, with a magnitude of $M_L \geq 5.5$).

Let us represent the intensities of these two streams of events as follows:

$$\lambda^{(\alpha)}(t) = b_0^{(\alpha)} + b_1^{(\alpha)} g^{(1)}(t) + b_2^{(\alpha)} g^{(2)}(t) \tag{8}$$

where $b_0^{(\alpha)} \geq 0, b_1^{(\alpha)} \geq 0, b_2^{(\alpha)} \geq 0$ are the parameters and $g^{(\beta)}(t)$ is the influence function of events $t_j^{(\beta)}$ of the flow with number β:

$$g^{(\beta)}(t) = \sum_{t_j^{(\beta)} < t} \exp(-(t - t_j^{(\beta)})/\tau) \tag{9}$$

Formula (9) sets the exponential decreasing the weight of the event with number j for times $t > t_j^{(\beta)}$ with relaxation time τ. The parameter $b_\beta^{(\alpha)}$ determines the measure of influence of the sequence β on the sequence α. The parameter $b_\alpha^{(\alpha)}$ gives the measure of self-exciting and the parameter $b_0^{(\alpha)}$ describes a purely random (Poisson) component of intensity. For a given parameter τ, let us consider the problem of estimating the parameters $b_0^{(\alpha)}, b_\beta^{(\alpha)}$ from maximizing the log-likelihood function for the time interval $[0, T]$ [39,40]:

$$\ln(L_\alpha) = \sum_{j=1}^{N_\alpha} \ln(\lambda^{(\alpha)}(t_j^{(\alpha)})) - \int_0^T \lambda^{(\alpha)}(s)ds, \quad \alpha = 1, 2 \tag{10}$$

Taking into account Formula (8), we can write the following:

$$\frac{\partial \ln(L_\alpha)}{\partial b_0^{(\alpha)}} = \sum_{j=1}^{N_\alpha} \frac{1}{\lambda^{(\alpha)}(t_j^{(\alpha)})} - \int_0^T ds, \quad \frac{\partial \ln(L_\alpha)}{\partial b_\beta^{(\alpha)}} = \sum_{j=1}^{N_\alpha} \frac{g^{(\beta)}(t)}{\lambda^{(\alpha)}(t_j^{(\alpha)})} - \int_0^T g^{(\beta)}(s)ds \tag{11}$$

Thus,

$$b_0^{(\alpha)}\frac{\partial \ln(L_\alpha)}{\partial b_0^{(\alpha)}}+\sum_{\beta=1}^{2} b_\beta^{(\alpha)}\frac{\partial \ln(L_\alpha)}{\partial b_\beta^{(\alpha)}}=\sum_{j=1}^{N_\alpha}\left\{\frac{b_0^{(\alpha)}+b_1^{(\alpha)}g^{(1)}(t_j^{(\alpha)})+b_2^{(\alpha)}g^{(2)}(t_j^{(\alpha)})}{\lambda^{(\alpha)}(t_j^{(\alpha)})}\right\}- \\ -\int_0^T (b_0^{(\alpha)}+b_1^{(\alpha)}g^{(1)}(s)+b_2^{(\alpha)}g^{(2)}(s))ds=N_\alpha-\int_0^T \lambda^{(\alpha)}(s)ds \tag{12}$$

Because the parameters $b_0^{(\alpha)}, b_\beta^{(\alpha)}$ are non-negative, terms on the left side of Formula (11) is equal to zero at the point of maximum of Function (10)—either due to the necessary conditions of the extremum (if the parameters are positive), or, if the maximum is reached at the boundary, then the parameters themselves are equal to zero. Consequently, at the point of maximum of the likelihood function, the equality is satisfied:

$$\int_0^T \lambda^{(\alpha)}(s)ds=N_\alpha \tag{13}$$

Let us substitute $g^{(\beta)}(t)$ from (9) into (13) and divide by T:

$$b_0^{(\alpha)}+\sum_{\beta=1}^{m} b_\beta^{(\alpha)}\cdot\overline{g}^{(\beta)}=\lambda_0^{(\alpha)}\equiv N_\alpha/T,\quad \overline{g}^{(\beta)}=\int_0^T g^{(\beta)}(s)ds/T \tag{14}$$

Substituting $b_0^{(\alpha)}$ from (14) into (10), we obtain the following maximum problem:

$$\Phi^{(\alpha)}(b_1^{(\alpha)},b_2^{(\alpha)})=\sum_{j=1}^{N_\alpha}\ln(\lambda_0^{(\alpha)}+\sum_{\beta=1}^{2} b_\beta^{(\alpha)}\cdot\Delta g^{(\beta)}(t_j^{(\alpha)}))\to\max \tag{15}$$

where $\Delta g^{(\beta)}(t)=g^{(\beta)}(t)-\overline{g}^{(\beta)}$, under the following restrictions:

$$b_1^{(\alpha)}\geq 0, b_2^{(\alpha)}\geq 0, \sum_{\beta=1}^{2} b_\beta^{(\alpha)}\overline{g}^{(\beta)}\leq\lambda_0^{(\alpha)} \tag{16}$$

The problem in (15) and (16) has a unique solution because Function (15) is convex with a negative definite Hessian. The problem in (15) and (16) is solved numerically for a given τ. After this, we can introduce the elements of the influence matrix $\kappa_\beta^{(\alpha)}, \alpha=1,2;\ \beta=0,1,2$ according to the following formulas:

$$\kappa_0^{(\alpha)}=b_0^{(\alpha)}/\lambda_0^{(\alpha)}\geq 0,\quad \kappa_\beta^{(\alpha)}=b_\beta^{(\alpha)}\cdot\overline{g}^{(\beta)}/\lambda_0^{(\alpha)}\geq 0 \tag{17}$$

The quantity $\kappa_0^{(\alpha)}$ is a pure stochastic share of the average intensity of the process $\lambda_0^{(\alpha)}$ with a number α, $\kappa_\alpha^{(\alpha)}$ is a self-excitation share $\alpha\to\alpha$ and $\kappa_\beta^{(\alpha)}$, $\beta\neq\alpha$ is a share of mutual influence $\beta\to\alpha$. The normalization condition is following from (17):

$$\kappa_0^{(\alpha)}+\kappa_1^{(\alpha)}+\kappa_2^{(\alpha)}=1,\quad \alpha=1,2 \tag{18}$$

As a result, we can determine the influence matrix:

$$\begin{pmatrix}\kappa_0^{(1)} & \kappa_1^{(1)} & \kappa_2^{(1)}\\ \kappa_0^{(2)} & \kappa_1^{(2)} & \kappa_2^{(2)}\end{pmatrix} \tag{19}$$

The stochastic shares of average intensities are given in the 1st column of the matrix (19). The right submatrix of size 2×2 consists of self-excited elements of average intensity on its diagonals, while the off-diagonal elements correspond to mutual excitation.

The model in (8) and (9) is a particular case of a Hawkes model of interactive point processes [41,42].

3.5. Relationship Between Local Maxima of the Instantaneous Amplitudes of Meteorological Parameters and Seismic Events

The further plan is to use the influence matrix apparatus to estimate the relationship between the times moments of largest local maxima amplitudes of the envelopes of meteorological time series and the time moments of strong earthquakes.

The threshold of local earthquake magnitudes for the Kamchatka Peninsula region in the KB GS RAS control zone was defined as $M_L \geq 5.5$. There were 418 such seismic events during the studied period (average recurrence of 15 events/year or 1.25 events/month).

The working hypothesis was investigated, which consisted in the fact that for some IMF levels of decomposition, the moments of time of the largest local maxima of the amplitudes of the envelope meteorological parameters "on average" precede the moments of time of earthquakes. In confirming this hypothesis, we assume that the maxima of meteorological parameters precede the occurrence of strong earthquakes, i.e., there is an effect of an advanced connection between meteorological parameters and strong earthquakes.

For a correct comparison of two event flows, their average intensities must be approximately equal. This means that the number of the largest local maxima of the amplitudes of the envelopes of meteorological parameter series must be equal to the number of earthquakes, i.e., 418. With an increase in the number of the IMF level, the amplitudes of their envelopes become lower and lower in frequency. As a result, it is possible to select the 418 largest local maxima of the amplitudes of the envelopes only for a certain number of lower decomposition levels.

As a result of sorting through the IMF levels for all three series of the EEMD decomposition (Figures 3–5), the 6th IMF level was chosen as the optimal one, for which the "direct" influence of the moments of time of the largest local maxima of the amplitudes of the envelopes on the moments of time of seismic events with a magnitude of at least 5.5 significantly exceeded the "reverse" influence.

This means that in the range of low instantaneous frequencies of the 6th level of decomposition, the amplitudes of the envelopes of meteorological time series precede the moments of time of sufficiently strong earthquakes and one can assume the presence of a prognostic effect.

Another possibility for extracting the amplitudes of the envelopes of narrow-band components of time series is to use wavelet decomposition with subsequent calculation of the amplitudes of the envelopes from each level of detail using the Hilbert transform. However, this method turned out to be less effective for studying the leading influence of meteorological parameters on seismic events than the Hilbert–Huang decomposition, with the exception of the air temperature time series. The behavior of the air temperature time series is quite smooth (Figure 1b), as a result of which the optimal Daubechies wavelet with 10 vanishing moments was determined for this time series from the condition of minimum entropy of the distribution of squares of wavelet coefficients [22]. The prognostic effect of such an analysis of the air temperature time series turned out to be most effective for the 6th detail level using wavelet decompositions. With a sampling time step of 3 h, this level corresponds to a range of periods of 8–16 days, that is, it is in the low-frequency range of 0.53–0.27 month^{-1}.

Figure 7a shows a sequence of earthquakes with magnitudes $M_L \geq 5.5$. Then, Figure 7b–d show the graphs of the envelope amplitudes at the 6th IMF level of the EEMD

decomposition of the time series of atmospheric pressure, air temperature and precipitation. In addition, Figure 7e shows the graph of the envelope amplitude of the wavelet decomposition of the air temperature time series at the 6th level of detail using the Daubechies wavelet with 10 vanishing moments.

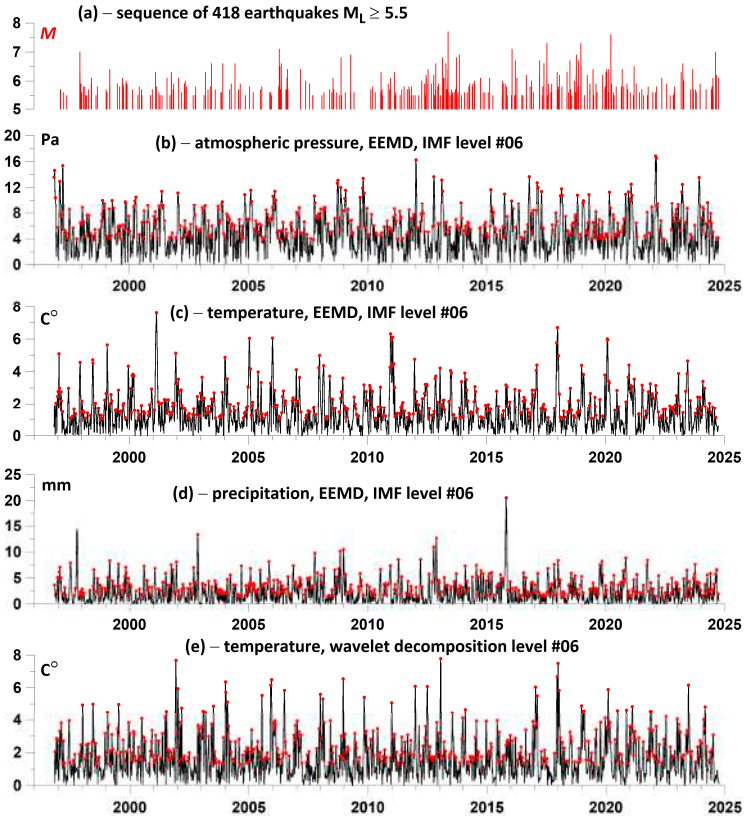

Figure 7. (**a**) Time sequence of 418 earthquakes with magnitude $M_L \geq 5.5$; (**b**–**e**) Results of calculating the amplitudes of the envelope for decompositions of the original time series: (**b**) for the 6th IMF level of decomposition of the atmospheric pressure series; (**c**) for the 6th IMF level of decomposition of the air temperature series; (**d**) for the 6th IMF level of decomposition of the atmospheric precipitation series; and (**e**) for the 6th level of wavelet decomposition of the air temperature series. The positions of the 418 largest local maxima of the envelope amplitudes are marked with red dots on each graph.

When analyzing variations in the components of influence matrices in sliding time windows corresponding to the mutual influence of the analyzed time sequences, the main attention is paid to their local maxima with their subsequent averaging. Below, we describe a method for processing these local maxima and averaging them for a set of time window lengths changing within specified limits.

1. Let us select the parameters, minimum $L_{\min}$ and maximum $L_{\max}$, of the lengths of time windows. Let N_L be the number of lengths of time windows in this interval. Thus, the lengths of time windows change according to the following formula: $L_k = L_{\min} + (k-1)\Delta L$ where $k = 1, \ldots, N_L$, $\Delta L = (L_{\max} - L_{\min})/(N_L - 1)$. In our calculations, we took $L_{\min}$ to be equal to 4 years, and $L_{\max}$ 7 years, where $N_L = 100$.

2. Each time window of length L_k is sliding along the time axis with some offset Δt. Let $t_j(L_k)$, $j = 1, \ldots, M(L_k)$ be the sequence of time moments of the positions of the right windows of length L_k. The number $M(L_k)$ of time windows of length L_k is determined by their time offset Δt. We used a time window offset Δt of 0.05 years.

3. The elements of the influence matrix (19) are estimated for a given relaxation time τ of the model in (8) and (9), corresponding to the mutual influence of the two analyzed processes for each position of time windows of the length L_k. In our calculations,

$\tau = 0.5$ years. For definiteness, we will consider some one influence, for example, of the first process on the second. As a result of such estimates, we obtain their values in the form $(t_j(L_k),\ c_j(L_k))$, where $c_j(L_k)$ is the corresponding element of the influence matrix for the position with the number j of the time window of length L_k.

4. In the sequence $(t_j(L_k),\ c_j(L_k))$, we select elements $(t_j^*(L_k),\ c_j^*(L_k))$ corresponding to the local maxima of values $c_j(L_k)$, that is, from the condition $c_{j-1}(L_k) < c_j^*(L_k) < c_{j+1}(L_k)$.

5. We choose a "small" time interval of length ε and for a sequence of such time fragments we calculate the average value of local maxima $c_j^*(L_k)$ for which their time marks $t_j^*(L_k)$ belong to these fragments. Averaging is performed over all lengths L_k, $k = 1, \ldots, N_L$ of time window. In our calculations, we took the length ε to be equal to 0.1 years.

Thus, the complete set of free parameters of the influence matrix method is τ, $L_{\min}$, $L_{\max}$, N_L, Δt, and ε.

4. Average Values of the Components of the Influence Matrices

Figure 8(a1–c1) shows the graphs of the average values of the components of the influence matrices of the sequence of the largest local maxima of the envelopes of time series of atmospheric pressure, air temperature and precipitation at the sixth IMF level of their EEMD decomposition into a sequence of earthquakes with a magnitude of $M_L \geq 5.5$ for 100 lengths of time window from 4 to 7 years.

Figure 8(d1) shows the graph of the average value of the influence matrices of the largest local maxima of the amplitudes of the envelope of the wavelet decomposition of the air temperature time series for the sixth detail level on earthquakes. Finally, Figure 8(e1) shows the "secondary" average value of all average components of the influence matrices in Figure 8(a1–d1).

The graphs in the right column of Figure 8(a2–e2) show all of the average values of the components of the influence matrices, corresponding to the "reverse" advance of the earthquake sequence on the positions of the largest local amplitudes of all time series of meteorological parameters.

The red lines in Figure 8 represent the average values for all time window positions in the range of window lengths from 4 to 7 years.

The graphs in Figure 8 show a pronounced leading (predictive) effect of the behavior of the amplitude maxima of the envelopes of meteorological time series in relation to seismic events. In this case, the maximum average value of the averaged components of the influence matrices of 0.426 was obtained for the air temperature time series (Figure 8(d1)). The inverse influence of seismic events on the behavior of meteorological parameter series is significantly lower, and for the air temperature series it becomes negligibly small (Figure 8(b2,d2)).

In all diagrams in the left column of the graphs in Figure 8, systematic bursts of the influence of local maxima of the amplitudes of the envelopes of time series of meteorological parameters on seismic events occur in 2011–2012, which preceded the seismicity activation in the Kamchatka Peninsula area in 2013, which included four strong seismic events, including the Sea of Okhotsk earthquake of 24 May 2013 with $M_W = 8.3$ (Table 1), which was the strongest seismic event during the period of detailed seismological observations in Kamchatka since 1962. In the individual diagrams in Figure 8(a1,d1,e1), this maximum can be traced from 2007, i.e., during the period of up to 6 years preceding the sharp increase in the activity of strong earthquakes in Kamchatka.

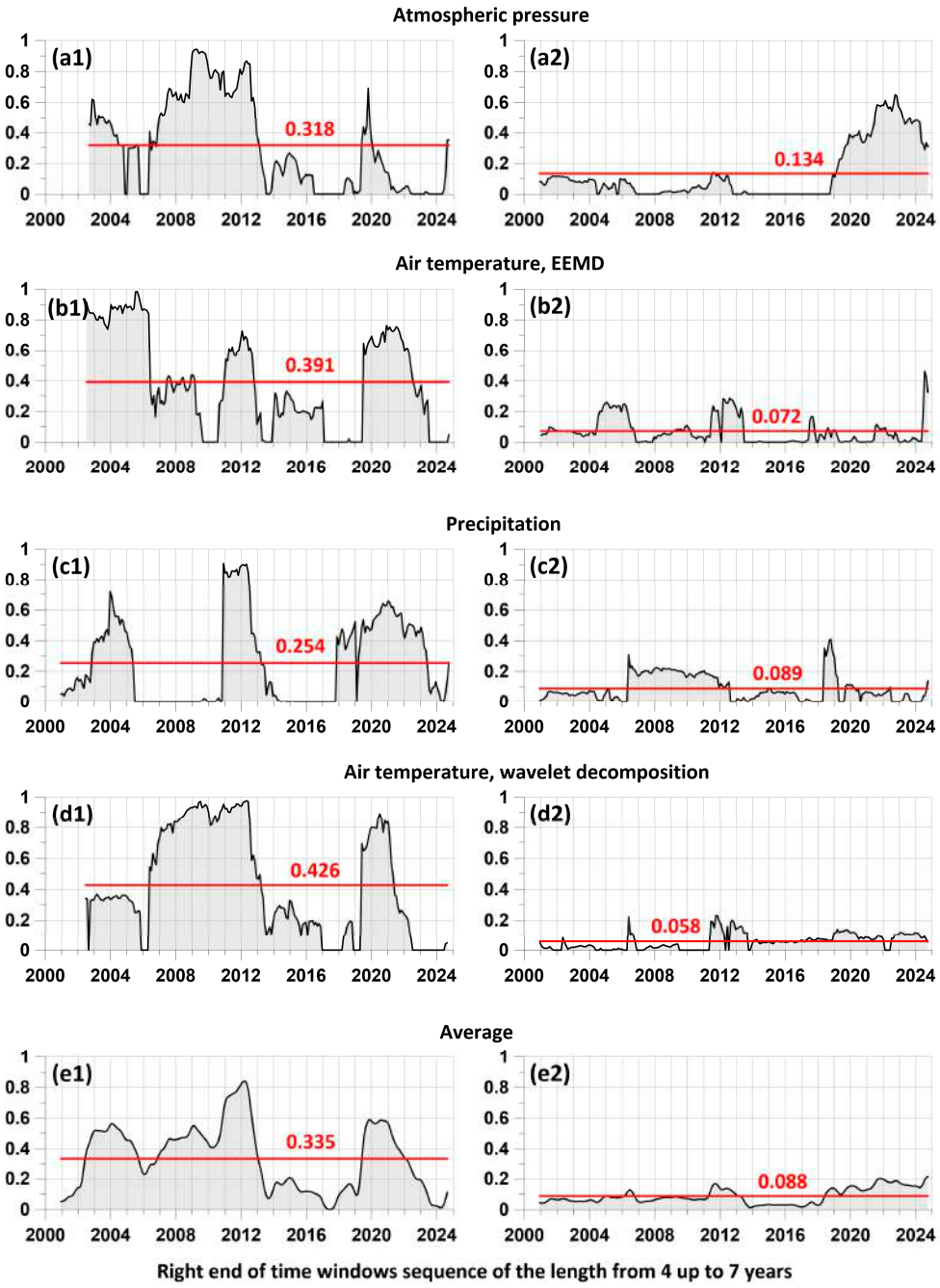

Figure 8. Average values of the components of the influence matrices of the largest local maxima of the amplitudes of the envelopes of meteorological parameter series on seismic events (left column of the graphs) and average values of the components of the reverse influence (right column of the graphs). The graphs (**a1**,**a2**) relate to "direct" and "reverse" influence matrices components between time moments of the biggest local maxima of atmospheric pressure instantaneous amplitudes at IMF level #6 and time moments of seismic events. The same is true for graphs (**b1**,**b2**) for air temperature; (**c1**,**c2**) for precipitation; and (**d1**,**d2**) again for temperature but at wavelet decomposition detail level #6 instead of IMF level #6. Graphs (**e1**,**e2**) present the averaging of all "direct" and "reverse" influence matrices components. The horizontal red lines represent the average values of the averaged components of the influence matrices for each meteorological parameter for the "direct prognostic" (left column of the graphs) and "reverse postseismic" (right column of the graphs) influence. The values of the average values are shown in red above each horizontal mean line. Figure 8 demonstrates a clear leading effect of meteorological anomalies before seismic events.

The next surge in the leading influence of the local maxima of meteorological parameters on the seismic process in 2019–2020 (Figure 8) preceded the earthquake of 25 March 2020 with a magnitude of $M_W = 7.5$ in the southern part of the considered area and the activation of seismicity immediately near the Pionerskaya meteorological station, including the earthquakes of 3 April 2023, $M_W = 6.5$ and 17 August 2024, $M_W = 7.0$ (Table 1), while the activation of seismicity in the northern part of the considered area in 2017–2018 was not accompanied by the leading manifestation of local maxima of meteorological parameters. This allows us to assume a certain connection between the manifestations of the discovered seismic prognostic effect of the advanced increase in the amplitudes of the envelope meteorological parameters with the relative proximity of earthquake foci and, possibly, with their seismotectonic localization.

The graph in Figure 8(e1) describes a strong averaging of the local maxima of the component of the influence matrices corresponding to the "direct" advance of the set of meteorological parameters of the local maxima of the moments of time of earthquakes with magnitudes of at least 5.5. In this case, averaging was performed for all three analyzed meteorological parameters, assuming that their changes occur in an interconnected manner and are controlled mainly by the advection of air masses due to their global movements in the Kamchatka Peninsula area.

At the same time, from the analysis of the left column of the graphs in Figure 8, it is evident that the local maxima of the envelopes of the precipitation series (Figure 8(c1)) demonstrate the least prognostic effect, compared to the atmospheric pressure and air temperature series. Therefore, the components of the influence matrices were averaged only for the atmospheric pressure and air temperature series. As a result, a graph was obtained (Figure 9), similar to that shown in Figure 8(e1), but with the exception of the precipitation time series.

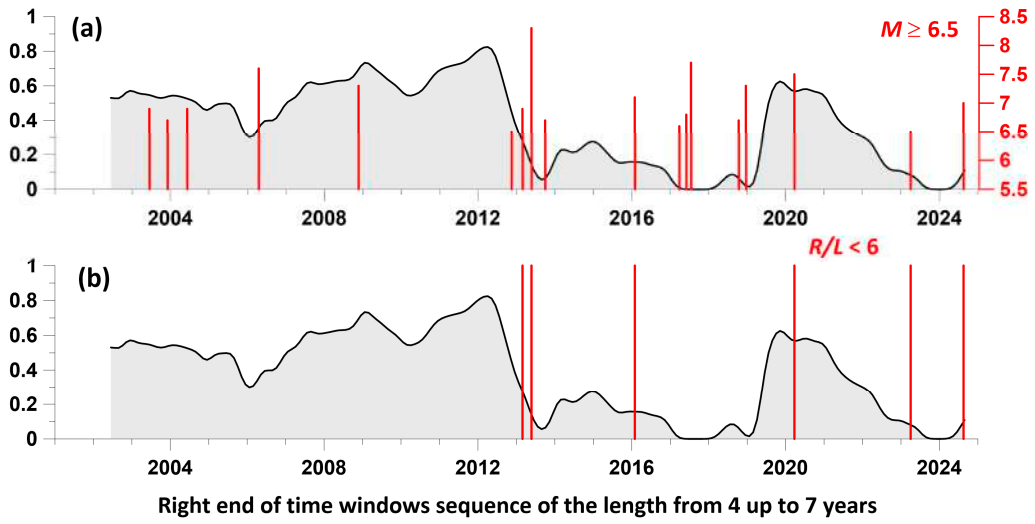

Figure 9. Gray lines present the average values of the components of the matrices of the influence of the largest local maxima of the amplitudes of the envelopes of atmospheric pressure and air temperature series (the precipitation time series is excluded) on seismic events in comparison with the time moments of earthquakes with magnitudes $M_W \geq 6.5$ (**a**) and the closest earthquakes for which the ratio of the epicentral distance R to the size of their source L is $R/L \leq 6$ (**b**). Vertical red lines indicate time moments and magnitudes (on the (a)) of seismic events.

5. Discussion

The graph in Figure 9 allows us to compare the behavior of the components of the averaged influence matrices for two time series of meteorological parameters both with the moments of the strongest earthquakes (Figure 9a) and taking into account the proximity of

the location of the foci of strong earthquakes in relation to the Pionerskaya meteorological station (Figure 9b).

To characterize the proximity of individual strong earthquakes in relation to the location of the weather station, we used the R/L ratio, where R is the epicentral distance to the Pionerskaya weather station, km; and L is the characteristic size of the earthquake source (in km) depending on its magnitude. The calculation of L was carried out using the formula $L = 10^{(0.43M_W - 1.27)}$ [24]. Thus, the R/L value (Table 1) shows the distance of the earthquake from the weather station in the number of earthquake source sizes and can be considered as an indicator of the intensity of the earthquake preparation process in the area of the weather station.

The lower panel of Figure 9 shows only those earthquakes for which the value of $R/L \leq 6$, i.e., when these earthquakes occurred, the meteorological stations were located within the middle (intermediate) zone of their sources. There were only six such earthquakes. These were the strongest events, which were accompanied in the area of the meteorological station by tremors with an intensity of 4 to 5–6 points on the MSK-64 scale, and for them the ratio $R/L = 2.3 - 5.4$.

Let us consider the manifestations of the maxima of the averaged graph of the components of the influence matrices of the largest local maxima of the amplitudes of the envelopes of the atmospheric pressure and air temperature series with the time distribution of the strongest earthquakes, as well as the closest of the strong earthquakes in relation to the weather station. It is evident that the manifestations of the local maxima of the graph precede the three strongest earthquakes with magnitudes $M_W = 8.3$, $M_W = 7.2$ and $M_W = 7.5$ with a characteristic lead time of such maxima of 1.5–2 years. The earthquakes of 2023 ($M_W = 6.5$) and 2024 ($M_W = 7.0$), which occurred at a relatively short distance from the weather station ($R/L = 3.6$ and $R/L = 2.3$), were not accompanied by preceding maxima in the changes in the components of the influence matrices. The same applies to the strong seismic events of 2017–2018, which occurred at distances of 450–800 km from the weather station within the junction of the Kuril–Kamchatka and Aleutian seismically active regions.

It should be concluded that the proposed method for identifying meteorological prognostic anomalies is mainly focused on the general seismic activity or, figuratively speaking, on the "seismic temperature" of the region. Therefore, identifying prognostic anomalies before specific strong earthquakes is not yet reliable and requires further research in this direction. In Figure 9, a strong non-stationarity of the average measure of the lead time of the greatest local maxima of instantaneous amplitudes relative to the time of the earthquake flow is noticeable. We believe that such non-stationarity is of interest for subsequent studies of its connection with cyclonic processes in the northern Pacific Ocean.

6. Conclusions

A method for analyzing the relationship between long-term meteorological observation data and the seismic process is proposed and implemented using the example of the Kamchatka seismically active region using the decomposition of meteorological time series by the Huang method and the construction of a sequence of orthogonal oscillations (intrinsic modes functions) for each series. Using the Hilbert transform, sequences of the distribution of instantaneous amplitudes were obtained from the sequence of these oscillation modes, which were compared with the moments of strong earthquakes within the framework of a parametric model of interacting point processes.

The most important result of the study is the detection of the effect of the advance of time points of maximum instantaneous amplitudes of air temperature, atmospheric pressure and precipitation of earthquake time moments at the low-frequency (sixth) IMF

level of Huang decomposition. This indicates the detection of the effect of an advance connection between changes in meteorological parameters, primarily air temperature, and the occurrence of strong earthquakes for characteristic periods of variation of 8–16 days.

The manifestation of maxima of average values of the components of the influence matrices of the largest local maxima of the amplitudes of the envelopes of atmospheric pressure and air temperature series was detected with a lead time of 1.5–2 years before three strong earthquakes in the Kuril–Kamchatka seismic active zone with magnitudes of 8.3, 7.2 and 7.5, which occurred at relative distances from the meteorological station of $R/L \leq 6$. To obtain more substantiated estimates of the seismic forecasting properties of the graphs of average values of the components of the influence matrices of the largest local maxima of the amplitudes of the envelopes of meteorological parameter series in relation to the strongest ($M_W \geq 6$) earthquakes in the region, as well as the closest of such earthquakes in relation to the observation area, it is necessary to conduct additional studies.

This article is still far from realizing the forecast of specific earthquakes based on the analysis of meteorological time series parameters with seismicity. An important point of subsequent studies should be the consideration of intensive atmospheric processes such as typhoons and cyclones. Formally, they can also be included in the assessment using the influence matrix method, not for pairs of point processes but for a multiple case.

Author Contributions: A.L.—ideating the research, writing the text, data processing; G.K.—writing the text; E.R.—data processing; Y.S.—data preparation. All authors have read and agreed to the published version of the manuscript.

Funding: This research received no external funding.

Institutional Review Board Statement: Not applicable.

Informed Consent Statement: Not applicable.

Data Availability Statement: The original meteorological data are contained in the database of the Kamchatka branch of the Geophysical Survey of the Russian Academy of Sciences: http://www.gsras.ru/new/infres/ (accessed on 15 December 2024), POLYGON Information System (Database of Geophysical Observations), ID 21. To obtain data for scientific research purposes, please contact G.N. Kopylova, co-author of this work, by e-mail: gala@emsd.ru.

Acknowledgments: This work was carried out within the framework of the state assignments of the Institute of Physics of the Earth of the Russian Academy of Sciences and Kamchatka branch of the Geophysical Survey of the Russian Academy of Sciences.

Conflicts of Interest: The authors declare that the research was conducted in the absence of any commercial or financial relationships that could be construed as a potential conflict of interest.

References

1. Dunajecka, M.A.; Pulinets, S.A. Atmospheric and thermal anomalies observed around the time of strong earthquakes in Mexico. *Atmosfera* **2005**, *18*, 235–247.
2. Genzano, N.; Filizzaola, C.; Hattori, K.; Pergola, N.; Tramutoli, V. Statistical correlation analysis between thermal infrared anomalies observed from MTSATs and large earthquakes occurred in Japan (2005–2015). *J. Geophys. Res. Solid Earth* **2021**, *126*, e2020JB020108. [CrossRef]
3. Hayakawa, M.; Izutsu, J.; Schekotov, A.; Yang, S.-S.; Solovieva, M.; Budilova, E. Lithosphere-atmosphere-ionosphere coupling effects based on multiparameter precursor observations for February–March 2021 earthquakes (M~7) in the offshore of Tohoku area of Japan. *Geosciences* **2021**, *11*, 481. [CrossRef]
4. Pulinets, S.A.; Boyarchuk, K.A. *Ionospheric Precursors of Earthquakes*; Springer: Berlin/Heidelberg, Germany, 2004; p. 288.
5. Ouzounov, D.; Pulinets, S.; Kafatos, M.C.; Taylor, P. Thermal Radiation Anomalies Associated with Major Earthquakes. In *Pre-Earthquakes Processes: A Multidisciplinary Approach to Earthquake Prediction Studies, AGU Geophysical Monograph Series*; John Wiley & Sons Inc.: New York, NY, USA, 2018; Volume 234, pp. 259–274. [CrossRef]

6. Pulinets, S.; Ouzounov, D. Lithosphere–Atmosphere–Ionosphere Coupling (LAIC) model—An unified concept for earthquake precursors validation. *J. Asian Earth Sci.* **2011**, *41*, 371–382. [CrossRef]
7. Ouzounov, D.; Pulinets, S.; Kafatos, M.C.; Taylor, P. (Eds.) *Pre-Earthquakes Processes: A Multidisciplinary Approach to Earthquake Prediction Studies, AGU Geophysical Monograph Series*; John Wiley & Sons Inc.: New York, NY, USA, 2018; Volume 234. [CrossRef]
8. Shitov, A.V.; Pulinets, S.A.; Budnikov, P.A. Effect of Earthquake Preparation on Changes in Meteorological Characteristics (Based on the Example of the 2003 Chuya Earthquake). *Geomagn. Aeron.* **2023**, *63*, 395–408. [CrossRef]
9. Cicerone, R.D.; Ebel, J.E.; Beitton, J.A. Systematic compilation of earthquake precursors. *Tectonophysics* **2009**, *476*, 371–396. [CrossRef]
10. Pulinets, S.A.; Ouzounov, D.P.; Karelin, A.V.; Davidenko, D.V. Physical bases of the generation of short-term earthquake precursors: A complex model of ionization-induced geophysical processes in the lithosphere-atmosphere-ionosphere-magnetosphere system. *Geomagn. Aeron.* **2015**, *55*, 521–538. [CrossRef]
11. Kuo, C.L.; Lee, L.C.; Huba, J.D. An Improved Coupling Model for the Lithosphere-Atmosphere-Ionosphere System. *J. Geophys. Res. Space Phys.* **2014**, *119*, 3189–3205. [CrossRef]
12. Lukianova, R.; Daurbayeva, G.; Siylkanova, A. Ionospheric and Meteorological Anomalies Associated with the Earthquake in Central Asia on 22 January 2024. *Remote Sens.* **2024**, *16*, 3112. [CrossRef]
13. Lukianova, R.; Christiansen, F. Modeling of the global distribution of ionospheric electric fields based on realistic maps of field-aligned currents. *J. Geophys. Res.* **2006**, *111*, A03213. [CrossRef]
14. Schekotov, A.; Borovleva, K.; Pilipenko, V.; Chebrov, D.; Hayakawa, M. Meteorological Response of Kamchatka Seismicity. In *Springer Proceedings in Earth and Environmental Sciences, Proceedings of the Problems of Geocosmos—2022 ICS 2022, St. Petersburg, Russia, 3–7 October 2022*; Kosterov, A., Lyskova, E., Mironova, I., Apatenkov, S., Baranov, S., Eds.; Springer: Cham, Switzerland, 2023. [CrossRef]
15. Uyeda, S.; Nagao, T.; Hattori, K.; Hayakawa, M.; Miyaki, K.; Molchanov, O.; Gladychev, V.; Baransky, L.; Chtchekotov, A.; Fedorov, E.; et al. Geophysical Observatory in Kamchatka region for monitoring of phenomena connected with seismic activity. *Nat. Hazards Earth Syst. Sci.* **2001**, *1*, 3–7. [CrossRef]
16. Konovalova, A.A.; Saltykov, V.A. Seismic Precursors of Large (M 6.0) Earthquakes in the Junction Zone between the Kuril-Kamchatka and Aleutian Island Arcs. *J. Volcanol. Seismol.* **2023**, *17*, 60–77. [CrossRef]
17. Gavrilov, V.A.; Panteleev, I.A.; Deshcherevskii, A.V.; Lander, A.V.; Morozova, Y.V.; Buss, Y.Y.; Vlasov, Y.A. Stress-Strain State Monitoring of the Geological Medium Based on The Multi-instrumental Measurements in Boreholes: Experience of Research at the Petropavlovsk-Kamchatskii Geodynamic Testing Site (Kamchatka, Russia). *Pure Appl. Geophys.* **2020**, *177*, 397–419. [CrossRef]
18. Kopylova, G.; Boldina, S. Hydrogeological Earthquake Precursors: A Case Study from the Kamchatka Peninsula. *Front. Earth Sci.* **2020**, *8*, 576017. [CrossRef]
19. Kopylova, G.N.; Serafimova, Y.K.; Lyubushin, A.A. Meteorological Anomalies and Strong Earthquakes: A Case Study of the Petropavlovsk-Kamchatsky Region, Kamchatka Peninsula. *Izv. Phys. Solid Earth* **2024**, *60*, 494–507. [CrossRef]
20. Kopylova, G.N.; Ivanov, V.Y.; Kasimova, V.A. The implementation of information system elements for interpreting integrated geophysical observations in Kamchatka. *Russ. J. Earth Sci.* **2009**, *11*, ES1006. [CrossRef]
21. Chebrova, A.Y.; Chemarev, A.S.; Matveenko, E.A.; Chebrov, D.V. Seismological data information system in Kamchatka branch of GS RAS: Organization principles, main elements and key functions. *Geophys. Res.* **2020**, *21*, 66–91. [CrossRef]
22. Chubarova, O.S.; Gusev, A.A.; Chebrov, V.N. The ground motion excited by the Olyutorskii earthquake of April 20, 2006 and by its aftershocks based on digital recordings. *J. Volcanol. Seismol.* **2010**, *4*, 126–138. [CrossRef]
23. Zelenin, E.; Bachmanov, D.; Garipova, S.; Trifonov, V.; Kozhurin, A. The Active Faults of Eurasia Database (AFEAD): The ontology and design behind the continental-scale dataset. *Earth Syst. Sci. Data* **2022**, *14*, 4489–4503. [CrossRef]
24. Zavyalov, A.D.; Zotov, O.D. A new way to determine the characteristic size of the source zone. *J. Volcanol. Seismol.* **2021**, *15*, 19–25. [CrossRef]
25. Huang, N.E.; Shen, Z.; Long, S.R.; Wu, V.C.; Shih, H.H.; Zheng, Q.; Yen, N.C.; Tung, C.C.; Liv, H.H. The empirical mode decomposition and the Hilbert spectrum for nonlinear and non-stationary time series analysis. *Proc. Roy. Soc. Lond. Ser. A* **1998**, *454*, 903–995. [CrossRef]
26. Huang, N.E.; Wu, Z. A review on Hilbert-Huang transform: Method and its applications to geophysical studies. *Rev. Geophys.* **2008**, *46*, RG2006. [CrossRef]
27. Bendat, J.S.; Piersol, A.G. *Random Data. Analysis and Measurement Procedures*, 4th ed.; Wiley & Sons: Hoboken, NJ, USA, 2010.
28. Mallat, S.A. *Wavelet Tour of Signal Processing*, 2nd ed.; Academic Press: Cambridge, MA, USA, 1999.
29. Huang, N.E.; Wu, M.; Qu, W.; Long, S.R.; Shen, S.S.P. Applications of Hilbert-Huang transform to non-stationary financial time series analysis. *Appl. Stoch. Models Bus. Ind.* **2003**, *19*, 245–268. [CrossRef]
30. Huang, Y.; Schmitt, F.G.; Lu, Z.; Liu, Y. Analysis of daily river flow fluctuations using empirical mode decomposition and arbitrary order Hilbert spectral analysis. *J. Hydrol.* **2009**, *373*, 103–111. [CrossRef]

31. Li, H.; Kwong, S.; Yang, L.; Huang, D.; Xiao, D. Hilbert-Huang Transform for Analysis of Heart Rate Variability in Cardiac Health. *IEEE/ACM Trans. Comput. Biol. Bioinform.* **2011**, *8*, 1557–1567. [CrossRef]
32. Wei, H.-C.; Xiao, M.-X.; Chen, H.-Y.; Li, Y.-Q.; Wu, H.-T.; Sun, C.-K. Instantaneous frequency from Hilbert-Huang transformation of digital volume pulse as indicator of diabetes and arterial stiffness in upper-middle-aged subjects. *Sci. Rep.* **2018**, *8*, 15771. [CrossRef]
33. Li, W.; Guo, J. Extraction of periodic signals in Global Navigation Satellite System (GNSS) vertical coordinate time series using the adaptive ensemble empirical modal decomposition method. *Nonlin. Process. Geophys.* **2024**, *31*, 99–113. [CrossRef]
34. Pan, Y.; Shen, W.-B.; Ding, H.; Hwang, C.; Li, J.; Zhang, T. The Quasi-Biennial Vertical Oscillations at Global GPS Stations: Identification by Ensemble Empirical Mode Decomposition. *Sensors* **2015**, *15*, 26096–26114. [CrossRef]
35. Pan, Z. Tornado Occurrence in the United States as Modulated by Multidecadal Oceanic Oscillations Using Empirical Model Decomposition. *Atmosphere* **2024**, *15*, 1257. [CrossRef]
36. Lyubushin, A.; Rodionov, E. Prognostic Properties of Instantaneous Amplitudes Maxima of Earth Surface Tremor. *Entropy* **2024**, *26*, 710. [CrossRef]
37. Lyubushin, A. Investigation of the Global Seismic Noise Properties in Connection to Strong Earthquakes. *Front. Earth Sci.* **2022**, *10*, 905663. [CrossRef]
38. Lyubushin, A.; Rodionov, E. Wavelet-based correlations of the global magnetic field in connection to strongest earthquakes. *Adv. Space Res.* **2024**, *74*, 3496–3510. [CrossRef]
39. Cox, D.R.; Lewis, P.A.W. *The Statistical Analysis of Series of Events*; Methuen: London, UK, 1966.
40. Daley, D.J.; Vere-Jones, D. *An Introduction to the Theory of Point Processes, Volume I: Elementary Theory and Methods*, 2nd ed.; Springer: New York, NY, USA, 2003.
41. Hawkes, A.G. Spectra of some self-exciting and mutually exciting point processes. *Biometrika* **1971**, *58*, 83–90. [CrossRef]
42. Laub, P.J.; Lee, Y.; Taimre, T. *The Elements of Hawkes Processes*; Springer International Publishing: Cham, Switzerland, 2021. [CrossRef]